# Nanoscale

Accepted Manuscript

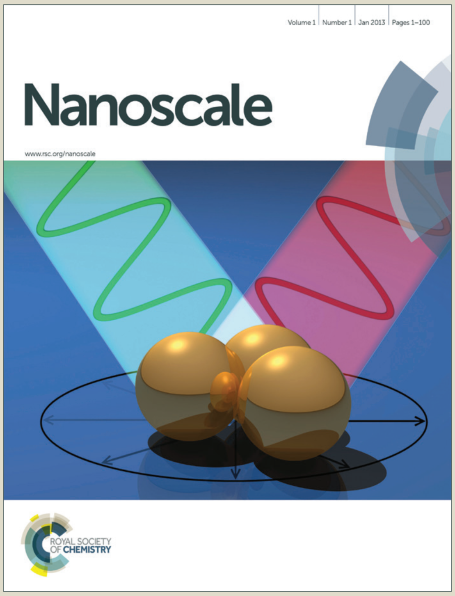

ROYAL SOCIETY OF CHEMISTRY

www.rsc.org/nanoscale

Cite this: DOI: 10.1039/c0xx00000x

www.rsc.org/xxxxxx

**ARTICLE TYPE**

# Well-dispersed Lithium Amidoborane Nanoparticles through Nanoreactor Engineering for Improved Hydrogen Release

**Guanglin Xia,‡ [a,b] Jie Chen,‡[a] Weiwei Sun,[c] Yingbin Tan,[a] Zaiping Guo*[b], Huakun Liu,[b] and Xuebin Yu*[a]**

***Received (in XXX, XXX) Xth XXXXXXXXX 20XX, Accepted Xth XXXXXXXXX 20XX***

**DOI: 10.1039/b000000x**

**Well-distributed lithium amidoborane (LiAB) nanoparticles are successfully fabricated *via* adopting carbon nanofibers (CNFs) with homogenous pores uniformly containing $Li_3N$ as the nanoreactor and reactant, simply prepared by a single-nozzle electrospinning technique, for the subsequent interaction with AB. The hierarchical porous structure consists of various macropores, mesopores and micropores *in-situ* produced during the formation of $Li_3N$ simultaneously serving as the reaction initiator, which not only controllably realizes the well-distribution of LiAB nanoparticles but also provides favorable channels for hydrogen release. By virtue of the hierarchical porous architecture and the nanoscale size effects, the LiAB nanoparticles start to release hydrogen at only 40 °C, which is 30 °C lower than that of pure LiAB, and dehydrogenate completely within only 15 min at 100 °C (10.6 wt.%). It provides a new perspective to the controllable fabrication of nanosized hydrogen storage materials.**

With global warming and environmental pollution caused by fossil fuels worsening, the development of alternative fuels is a matter of great importance. Hydrogen as a promising green energy with great advantages of high gravimetric energy density (142 MJ $kg^{-1}$), widely available sources, light weight and environmental friendliness is attracting more and more attention.[1] Developing suitable hydrogen storage materials satisfying all the criteria, however, has been a key technological challenge for the widespread use of hydrogen.[2-5]

Many recent efforts have been directed towards the development of chemical hydrides as promising hydrogen storage media.[6] Among them, ammonia borane (AB) is an excellent candidate for hydrogen storage owing to the ultrahigh hydrogen capacity (19.6 wt.%), satisfactory air stability, and relatively low molecular mass (30.7 g $mol^{-1}$).[7, 8] The direct use of pristine AB as a hydrogen energy carrier, however, is hindered by the long induction period, slow decomposition rate in the first step at 100 °C and the concurrent release of volatile by-products (*e.g.*, borazine, diborane and aminodiborane).[9-12] Interestingly, by the replacement of one H from AB with metal ions, the thus-formed metal amidoboranes show the significantly enhanced dehydrogenation kinetics and suppressed volatile by-products, due to the iconicity change of N-H and B-H bond introduced by the related metal ions.[13-22] Especially, lithium amidoborane (LiAB) with high hydrogen capacity (13.7 wt.%) and accessible low temperature is standout from other materials to be an appropriate candidate.[23, 24] Nonetheless, similar with the dehydriding behavior of AB, the dehydriding rate of LiAB at low temperature is still low for practical application, especially for the second-step dehydrogenation that may be attributed to the sluggish diffusion of both positive and negative hydrogen across the reactive solid interfaces.[25]

Recent theoretical calculations and experiments have demonstrated that the nanoscaled structure offers hydrogen storage materials a shorter diffusion path length, the larger specific surface area and the decreased thickness of reactive interfaces during $H_2$ ab-/desorption process.[26-31] Moreover, the excess of surface energy occurring in small particles could facilitate the material's destabilization.[32] These advantages are capable of enhancing the thermodynamics and kinetics of dehydrogenation.[33-38] In particular, by confining AB in various porous templates, *e.g.*, metal organic frameworks,[39-41] mesoporous carbon,[42] silica hollow nanospheres,[43] and mesoporous boron nitride,[44] the significantly improved dehydrogenation kinetics at lower temperature and the complete suppression of volatile by-products have been successfully realized. Inspired by this method, constructing the nanosized LiAB might be a feasible route to improve its kinetics and thermodynamics for hydrogen release. To fabricate nanosized complex hydrides, considerable efforts have been devoted to impregnating them into various porous matrixes, which can not only directly synthesize the nanostructured composites but also physically hinder the agglomeration during thermal treatment for hydrogen desorption.[27, 28] During the infiltration process into mesoporous templates, the pores with relatively small sizes, however, are easier to be blocked more or less, which results in terrible encapsulation and agglomeration of reactive substrates.[45] Additionally, it is still of a big challenge to keep the thus-formed nanoparticles separated *via* the method of nanoconfinement so the agglomeration and particle growth during thermal dehydrogenation is inevitable.[46] Right now, facile control over the spatial distribution of precursors inside the scaffolds is largely lacking with existing strategies.

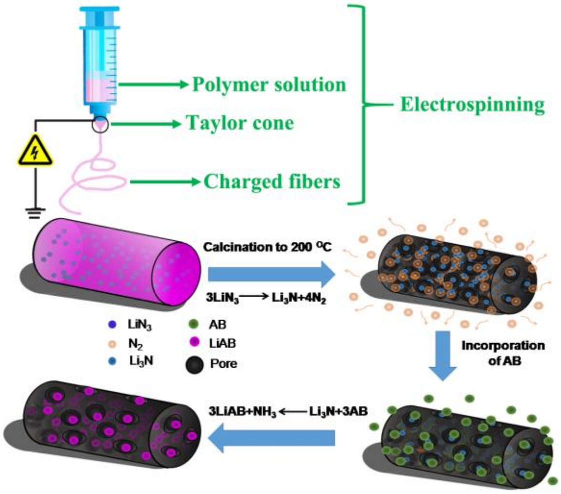

Scheme 1. Schematic illustration of the synthetic procedure of the LiAB@CNFs.

It should be noted that the low solubility of LiAB with lack of melting nature even makes traditional infiltration method unrealizable up to now. In order to achieve the synthesis of nanoconfined LiAB nanoparticles with effective infiltration and well-distribution, we established a simple and highly effective method using the reaction between AB and $Li_3N$ well-distributed in the porous CNFs to produce uniformly distributed LiAB nanoparticles with improved dehydrogenation properties. As schematically illustrated in Scheme 1, we firstly fabricated PVA-coated $LiN_3$ nanofibers using PVA-$LiN_3$ mixture as the precursor by a simple electrospinning technique. By successive calcination of the thus-formed nanofibers, a plenty of micropores, mesopores and macropores were generated upon the explosive release of $N_2$ from $LiN_3$ accompanied by the carbonization of PVA. It *in-situ* produces the $Li_3N$ nanoparticles with well-distribution space-confined inside the separated pores and sufficient space for the accommodation of AB to interact with $Li_3N$.[46] Firstly, the three-dimensionally distributed porous carbon matrixes possess a large plenty of macropores between individual CNFs, providing favorable diffusion pathway for the effective infiltration of the precursors into the "nanoreactor". Secondly, during the reaction, each $Li_3N$ nanoparticle serving as an active site separated by porous carbon shell inside the CNFs initiates the formation of LiAB *via* the reaction with AB with a molar ratio of 1:3 under the steric hindrance of carbon coating, simultaneously realizing the controllable synthesis of LiAB with high loading, well dispersion and robust stability. In addition, owing to the mechanical support of carbonaceous frameworks, the morphology of porous CNFs was well maintained during the whole reaction process and thermolysis process, which is able to effectively stabilize the physical environment of LiAB.

Figure 1a shows an overall SEM morphology of the as-electrospun nanofibers. It demonstrates that the as-synthesized PVA-coated $LiN_3$ fibers are continuous with quite smooth surface and a relatively uniform diameter distribution of ~200 nm. After calcination to 550 °C, the uniform fibrous nanostructure is well preserved and the average diameter was decreased to ~150 nm resulting from the huge mass loss of PVA upon carbonization (Figure 1b). The relatively high-magnification SEM images clearly illustrate that the previous smooth surface turns to be rough and is filled with both mesopores and macropores with various diameters (5–50 nm) (Figure 1c) due to the strong release of $N_2$ from the decomposition of $LiN_3$. Moreover, the SEM image of an occasionally broken fiber (highlighted by the red circle in Figure 1c) verified the presence of mesopores inside the CNFs. This is attributed to the well-distribution of $LiN_3$ in the as-electrospun PVA nanofibers. Numerous mesopores can be directly observed in the TEM image (Figures 1e), confirming the 3D porous architectures of the as-prepared carbon-coated $Li_3N$ nanofibers ($Li_3N$@CNFs). The highly porous structure of the $Li_3N$@CNFs is further illustrated by the $N_2$ adsorption-desorption

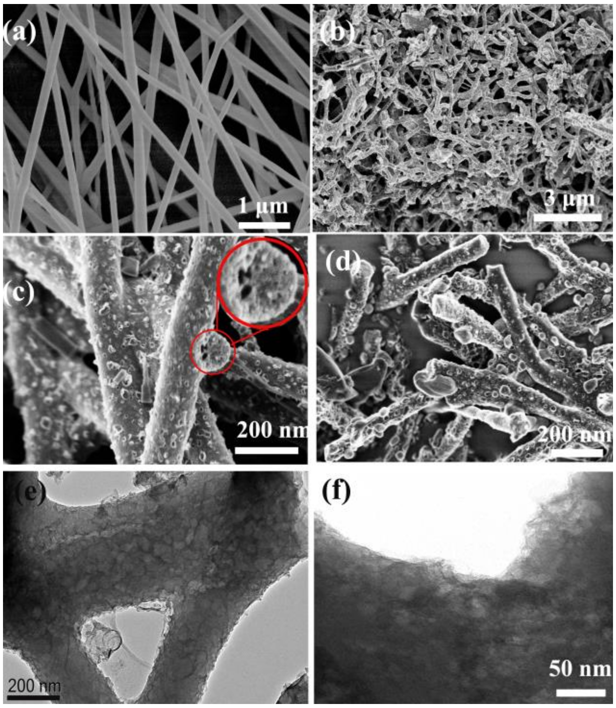

Figure 1. SEM images of (a) the as-electrospun PVA-coated $LiN_3$ nanofibers, (b) the as-prepared $Li_3N$@CNFs and its large magnification image (c). (d) SEM images of the LiAB@CNFs. TEM images of $Li_3N$@CNFs (e) and LiAB@CNFs (f).

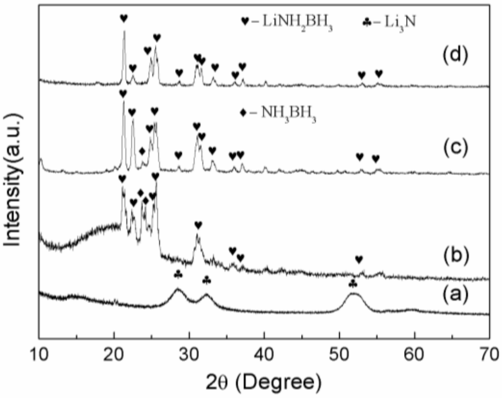

Figure 2. XRD patterns of the as-prepared $Li_3N$@CNFs (a), LiAB@CNFs (b), including the products of $Li_3N$ and AB *via* the wet-chemical method (c) and referenced LiAB (d) for comparison.

plots (Figure S1). From the plots, an obvious absorption was observed both at high relative pressure and low pressure, demonstrating the existence of large size pores and micropores, respectively. In addition, there is a broad distribution between 2 nm and 50 nm in the pore size distribution results, which agrees well with the SEM and TEM results. Hence, it confirms that the CNFs are hierarchically full of micropores, mesopores and macropores. The multiple and interconnected pores are favorable for the encapsulation of AB thoroughly, and, more importantly, they can simultaneously offer sufficient room around each $Li_3N$ nanoparticles inside the nanoreactor for the subsequent reaction. After the infiltration of AB, the morphology of CNFs is well-maintained during the whole reaction process as evidenced by the SEM image in Figure 1d. Nonetheless, comparing to the as-prepared CNFs, no obvious pores are observed after the interaction with AB from TEM image (Figure 1f), indicating that most of the mesopores have been filled up. Moreover, both the BET surface area and the cumulative pore volume of the CNFs is substantially reduced resulting from the encapsulation of AB, concurrent with a significant reduction of the intensity of the Barrett-Joyner-Hallenda (BJH) pore size distribution. It undoubtedly demonstrates that AB penetrates the porous network of CNFs and occupies a large fraction of the pores and/or blocks the pores. Furthermore, it should be noted that the formation of LiAB is initiated by the interaction of AB with the pre-existing $Li_3N$ nanoparticles, which therefore ensures the well-distribution of the thus-formed LiAB particles.

In the XRD results as shown in Figure 2, characteristic peaks of LiAB, which is similar with LiAB produced from the reaction between LiH and AB *via* ball-milling,[23] are present for the as-formed composites from the interaction of $Li_3N$ with AB in THF. It therefore verifies the feasibility to synthesize LiAB by this wet-chemical reaction.[47] After the interaction of the CNFs containing $Li_3N$ with the solution of AB, the peaks belonging to LiAB appeared along with the disappearance of $Li_3N$ (Figure 2a). It directly confirms the stabilization of LiAB inside during the reaction process. Some peaks belonging to $NH_3BH_3$ were also observed in the product. This may result from the insufficient washing of the CNFs. Moreover, it can be seen that the peaks attributed to LiAB inside the CNFs are broader than that of pure LiAB, suggesting the smaller crystallite dimension of LiAB owing to the nanoconfinement effects. The average particle size of LiAB, calculated from Debye-Scherrer's equation, is ~ 25.3 nm. The presence of the characteristic peaks of N-H and B-H bonds assigned to LiAB for the LiAB@CNFs was further confirmed by FTIR spectra (Figure S2). Besides, it is observed that, in the whole spectrum, the peaks assigned to PVA disappeared after carbonization only with the presence of LiAB, suggesting the chemical inertness of the CNFs that only serves as the nanoreactor.

To explore the nanosize effects on the hydrogen storage properties, a comparison of the thermal decomposition performance of the as-prepared LiAB@CNFs, with the ball-milled LiAB and LiAB/CNFs composite as control sample, was conducted by employing TG and MS in tandem with volumetric measurements. As shown in Figure 3, the decomposition process of bulk LiAB could be divided into two steps. The onset and peak temperature of the first step desorption were 70 °C and 98 °C, respectively, and the second step began at 120 °C with a peak at 150 °C, which agrees well with the TG results. In addition, the total weight loss was 10.2 wt.% with a gradual decomposition during the second stage, corresponding well with previous reports.[14, 23, 24, 48] In the case of the ball-milled LiAB/CNFs mixture, it underwent a decomposition process starting at 50 °C and ceasing at 180 °C with a broader decomposition temperature range compared with LiAB, giving a weight loss of ~10.2 wt.% similar to pure LiAB. Therefore, it could be concluded that the carbonaceous materials have no effects on facilitating the kinetics of hydrogen release. In contrast, the as-prepared LiAB@CNFs showed a one-step decomposition with the onset and peak temperature of $H_2$ desorption downshifted to~40 °C and 80 °C, respectively, which were 30 °C and 20 °C lower than that for the first step reaction of pure LiAB. The one-step desorption of LiAB@CNFs was also observed from the MS curve, suggesting that the decomposition route of LiAB may be changed owing to the nanoconfinement effects. It is similar with the observation of the nanoconfinement effects on the decomposition of AB.[39, 41, 43, 49, 50] Furthermore, TG results illustrated that most of $H_2$ was quickly released before 105 °C, in concurrence with the MS spectra, which performed much higher desorption rate under the same weight loss ( ~10.5 wt.%) compared with bulk LiAB. Moreover, the weight loss is in good agreement with the volumetric results, confirming the high-purity of the released hydrogen from LiAB@CNFs (Figure S3). All the remarkable desorption performance verifies that the carbon-coated LiAB nanofibers through nanoreactors engineering improved the hydrogen desorption kinetics.

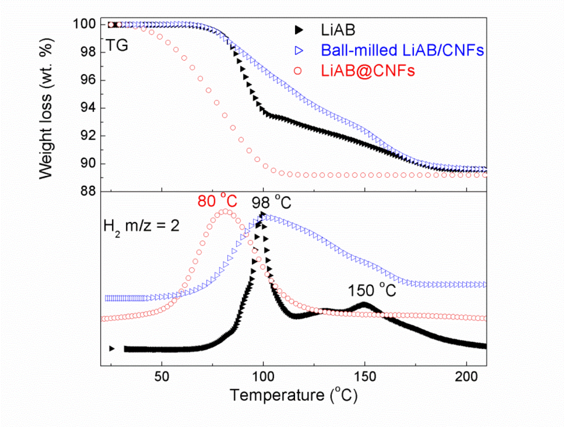

Figure 3. TG and MS results for bulk LiAB, ball-milled LiAB/porous carbon, and LiAB@CNFs, with a heating rate of 5 °C/min. $H_2$ storage capacity is normalized to the LiAB in the composite.

Insights into the dehydrogenation kinetics of LiAB@CNFs and bulk LiAB were gained by applying the volumetric desorption measurements at different temperatures (Figure 4 and Figure S4). As shown in Figure 4, even at a high temperature of ~100 °C, the bulk LiAB exhibits a hydrogen release of ~7 wt.% within 60 min. By contrast, the LiAB nanoparticles are able to release~7.5 wt.% hydrogen at a temperature as low as 60 °C through the same operation time. Apparently, with increasing operation temperature, faster kinetics is yielded for the LiAB@CNFs. Specifically, upon further elevating the temperature to 80 and 90 °C, hydrogen capacities of 8.7 and 9.5 wt.% could be observed,

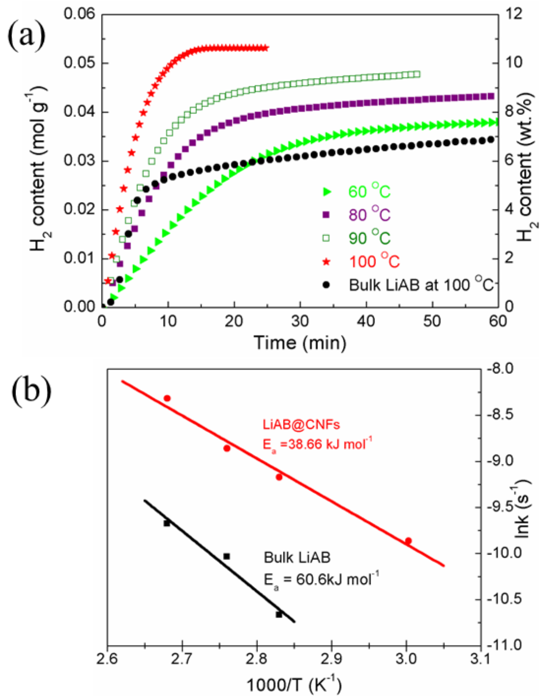

Figure 4. (a) Hydrogen desorption curves of the LiAB@CNFs at different temperatures, including bulk LiAB at 100 $^{o}$C for comparison. Carbon was not considered as an active component for the hydrogen storage measurements; (b) Arrhenius plot according to the isothermal $H_2$ desorption of the LiAB@CNFs and bulk LiAB.

respectively. The value can further reach to ~10.6 wt.%, approaching its theoretical releasable capacity, at 100 $^{o}$C in less than 15 min. For a quantitative evaluation of the enormously improved dehydriding kinetics of the as-prepared LiAB@CNFs, the apparent activation energy ($E_a$) was calculated from various isothermal dehydrogenation results *via* linear Arrhenius plots of ln$k$, ($k$, rate constant), as a function of 1/$T$ ($T$, absolute temperature). Figure 4(b) displays the details for calculation of apparent activation energies. It gives the activation energies of approximately 38.7 kJ mol$^{-1}$ and 60.6 kJ mol$^{-1}$ for the LiAB nanoparticles and bulk counterpart, respectively. The activation energies of pure LiAB is a little different from the value reported previously (75 kJ mol$^{-1}$),[51] possibly attributed to the various fabrication method involved. The significant decrease of activation energy gives a direct evidence of the improvement of hydrogen release kinetics resulting from the nanoconfinement and the nanoporous structure.

The XRD pattern of LiAB@CNFs after decomposition to 120 $^{o}$C (Figure S5) demonstrates the formation of an amorphous phase, which is similar with the bulk LiAB due to the polymerization occurring between N-H bonds and B-H bonds. Further information on the decomposition pathway was therefore provided by the FTIR spectra (Figure S2). It verifies the disappearance of N-H bonds and a dramatic decay of B-H bonds in both bending and stretching modes with the appearance of B-N bonds of LiAB@CNFs after dehydrogenation to 120 $^{o}$C. It indicates the complete dehydrogenation of LiAB nanoparticles owing to the interaction of B-H and N-H bonds. The weak peaks indexed to B-H bonds are attributed to the formation of a small amount of $BH_4$ group upon the thermolysis of LiAB, which is normally formed in the dehydrogenation of metal amidoboranes.[23, 52] Nonetheless, both N-H and B-H bonds are clearly observed for the bulk LiAB upon decomposition at 120 $^{o}$C and disappeared until heating to 250 $^{o}$C for a full dehydrogenation (Figure S6). It provides further evidence for the improved dehydrogenation kinetics of LiAB *via* stabilization inside the CNFs.

To understand the effects of nanoconfinement on the thermodynamics and reversibility of LiAB, DSC was employed to monitor the enthalpy change during dehydrogenation (Figure S7). It is noted that the hydrogen release process from LiAB@CNFs is still exothermic with an enthalpy change of -6.68 kJ mol$^{-1}$ $H_2$, slightly less exothermic than that of pure LiAB (-7.83 kJ mol$^{-1}$). Although the reduced exothermicity could benefit the hydrogenation of the decomposition products of LiAB, no reversible phenomenon has been observed via solid-gas reaction under 10 MPa $H_2$ pressure at various temperatures due to the exothermic reaction between N-H and B-H for hydrogen desorption.

In summary, we established a simple and effective method, using mesopores *in-situ* formed during the formation of $Li_3N$ as nanoreactors to support the reaction between AB and $Li_3N$, to synthesize the LiAB nanoparticles with well-dispersion and nanometer size. Porous $Li_3N$ nanofibers not only were used as reactant to synthesize and stabilize LiAB, but also offered sufficient room and channels for the successive transportation and reaction. Taking advantage of the special architecture of the porous CNFs and the reaction mechanism between $Li_3N$ and AB, the high loading capacity and well dispersion of LiAB were simultaneously realized. Due to the physical confinement effects, the growth of LiAB crystal is largely controlled. The nanosized LiAB particles present significantly enhanced hydrogen desorption properties with the rapid release of 10.6 wt.% hydrogen in 15 min at 100 $^{o}$C. The special methodology for stabilizing LiAB nanoparticles provides a viable strategy for synthesizing other nanostructured metal amidoborane towards improved hydrogen storage properties.

## Acknowledgements

This work was partially supported by the Ministry of Science and Technology of China (2010CB631302), the National Natural Science Foundation of China (21271046), the PhD Programs Foundation of the Ministry of Education of China (20110071110009), and the Science and Technology Commission of Shanghai Municipality (11JC1400700). Z. Guo acknowledges a Discovery Project (DP140102858) from the Australia Research Council.

## Experimental sections

### Synthesis of 3D $Li_3N$@CNFs

Poly(vinylalcohol ) (0.5 g, Alfa Aesar, Mv=88000, CAS:9002-89-5) was mixed with deionized water (5 ml) and stirred in oil bath at 40 °C over night. After PVA molecules were fully swelled in water, then turn the temperature to the 90 °C for 8 h to make a well-proportioned and stable PVA solution. $LiN_3$ solution(0.4

mL, 20 wt.%) in water was then added into the cooled PVA solution and vigorously stirred for 6 h to make a homogeneous spinning dope. The well-prepared precursor solution was poured into a syringe with an 18-gauge blunt tip needle. Set the voltage as 15KV which was provided by a high–voltage power supply between the needle and the collector. Also the flow rate of solution was approximately 500 μL $h^{-1}$ controlled by a syringe pump (Longer, TJP-3A, China), and a grounded stainless steel plate was horizontally placed 10 cm from the needle to collect the nanowires. The as-collected fibers by electrospinning were firstly dewatered in the 75 °C water bath under dynamic vacuum for 15 h. Then the successive calcinations to 550 °C for 3 h was taken under dynamic $N_2$ atmosphere with a pressure of ~ 1 bar to obtain the 3D nanoporous carbon-coated $Li_3N$ fibers with a heat rate of 2 °C $min^{-1}$.

**Synthesis of 3D porous LiAB@CNFs**

The thus-formed $Li_3N$@CNFs was then immersed into the solution of AB in THF in the glove box for ~4 h. The mixture was then ultrasonicated for ~5 min at room temperature for several times, and, subsequently, the CNFs in the form of film was then taken out and washed with pure THF for several times to remove the residual AB. Finally, the CNFs was treated under vacuum for ~ 12 h to remove solvent and yield the carbon-coated LiAB nanofibers (LiAB@CNFs)**.** The mass concentration of LiAB in the as-prepared fibers, which was calculated to be 52.1 wt.%, was obtained by elemental analysis.

**Preparation of LiAB powders**

$Li_3N$ (99.4 wt.%) and AB (97 wt.%) were commercial products and used as received. Tetrahydrofuran (THF) was purified by distilling with sodium-potassium alloy under an inert Ar atmosphere. AB (200 mg) was dissolved in THF (20 mL) under magnetic stirring for 3 min. $Li_3N$ powder (75.2 mg) was added into AB solution in the golvebox. Then the mixture was allowed to react for 60 min at 30 $^oC$ under the Ar atmosphere. At the end of the reaction, the white LiAB powder was obtained by vacuum drying the solution overnight at room temperature. All the samples were handled in a glove-box filled with Ar (99.9999%), which was equipped with a circulative purification system to control the $H_2O/O_2$ levels below 0.1 ppm. The reaction involved for the production of LiAB can be expressed in eq. (1).

$$3\ NH_3BH_3 + Li_3N \rightarrow 3LiNH_2BH_3 + NH_3 \quad (1)$$

**Synthesis of LiAB/CNFs composite by ball-milling**

In this case, the as-synthesized LiAB was mixed with CNFs in a weight ratio of 1:1 by ball milling for 2 h to form a mixture for the further experimental trials. The ball milling was performed on a planetary ball mill (QM-1SP2, Nanjing) with a ball-to-powder weight ratio of 30: 1 and a rotating speed of 350 rpm. Due to the relatively lower onset temperature of decomposition (approximately 80 $^oC$), the milling procedure was carried out by alternating between 6 min of milling and 6 min of rest. In order to prevent contamination by air, all handling and manipulation of the materials were performed in an argon-filled glove box.

**Materials characterization**

Dehydrogenation of the ball-milled LiAB/CNFs composite, LiAB@CNFs and the bulk LiAB composite were characterized by temperature-programmed desorption (TPD) performed on a Sieverts-type apparatus, connected to a reactor filled with sample (0.04g) under argon atmosphere (1 bar) at a heating rate of 5 $^oC$ $min^{-1}$. Simultaneous thermogravimetric analysis and mass spectrometry (TGA-MS, Netzsch STA 449C) were conducted at room temperature, using a heating rate of 5 $^oC$ $min^{-1}$ under dynamic argon with a purge rate of 80 mL $min^{-1}$. Differential scanning calorimetry (DSC) measurements were performed by TAQ 2000 DSC under argon with a gas flow of 40 mL Ar $min^{-1}$ at a heating rate of 5 $^oC$ $min^{-1}$. Nitrogen absorption/desorption isotherms (Brunauer–Emmett–Teller39 (BET) technique) at the temperature of liquid nitrogen *via* a Quantachrome NOVA 4200e instrument were collected to characterize the pore structure of the samples. The phase composition of the powders was analyzed by X-ray diffraction (D8 Advance, Bruker AXS) with Cu Kα radiation. Amorphous tape was used to prevent any possible reactions between the sample and air during the XRD measurement. Fourier transform infrared (FTIR, Magna-IR 550 II, Nicolet) analysis was conducted to determine the chemical bonding. During the FTIR measurements (KBr pellets), samples were loaded into a closed tube with KBr for measurement in the argon-filled glove box. The morphology of the samples was evaluated using a field emission scanning electron microscope (FE-SEM, JEOL 7500FA, Tokyo, Japan) and a transmission electron microscope (TEM, JEOL 2011 F, Tokyo, Japan), operating at 1keV and 200 keV, repectively.

## Notes and references

[a] *Department of Materials Science, Fudan University, Shanghai, China. E-mail: yuxuebin@fudan.edu.cn*
[b] *Institute for Superconducting and Electronic Materials, University of Wollongong, Wollongong, Australia. E-mail: zguo@uow.edu.au*
[c] *Department of Chemical Engineering, Shanghai University, Shanghai, China*

† Electronic Supplementary Information (ESI) available: Supplementary figures of BET, XRD, TPD and FTIR reults. See DOI: 10.1039/b000000x/

‡ These authors contributed equally to the work.

1. L. Schlapbach and A. Zuttel, *Nature*, 2001, **414**, 353.
2. U. Eberle, M. Felderhoff and F. Schuth, *Angew. Chem.-Int. Ed.*, 2009, **48**, 6608.
3. M. Yadav and Q. Xu, *Energy Environ. Sci.*, 2012, **5**, 9698.
4. H.-L. Jiang , S. K. Singh , J.-M. Yan , X.-B. Zhang and Q. Xu, *ChemSusChem*, 2010, **3**, 541.
5. Z.-H. LU and Q. Xu, *Funct. Mater. Lett.*, 2012, **05**, 1230001.
6. S.-i. Orimo, Y. Nakamori, J. R. Eliseo, A. Züttel and C. M. Jensen, *Chem. Rev.*, 2007, **107**, 4111.
7. Z. G. Huang and T. Autrey, *Energy Environ. Sci.*, 2012, **5**, 9257.
8. A. Staubitz, A. P. M. Robertson and I. Manners, *Chem. Rev.*, 2010, 110, 4079.
9. P. Wang, *Dalton Trans.*, 2012, **41**, 4296.
10. H. K. Lingam, X. Chen, J.-C. Zhao and S. G. Shore, *Chem. Euro. J.*, 2012, **18**, 3490.
11. X. Chen, X. Bao, J.-C. Zhao and S. G. Shore, *J. Am. Chem. Soc.*, 2011, **133**, 14172.
12. R. Chiriac, F. Toche, U. B. Demirci, O. Krol and P. Miele, *Int. J. Hydrogen Energy*, 2011, **36**, 12955.
13. Y. S. Chua, P. Chen, G. Wu and Z. Xiong, *Chem. Comm.*, 2011, **47**, 5116.
14. H. Wu, W. Zhou and T. Yildirim, *J. Am. Chem. Soc.*, 2008, **130**, 14834.
15. A. T. Luedtke and T. Autrey, *Inorg. Chem.*, 2010, **49**, 3905.
16. G. L. Xia, Y. B. Tan, X. W. Chen, Z. P. Guo, H. K. Liu and X.

B. Yu, *J. Mater. Chem. A*, 2013, **1**, 1810.

17. X. Kang, J. Luo, Q. Zhang and P. Wang, *Dalton Trans.*, 2011, **40**, 3799.
18. H. Wu, W. Zhou, F. E. Pinkerton, M. S. Meyer, Q. Yao, S. Gadipelli, T. J. Udovic, T. Yildirim, J. J. Rush, *Chem. Comm.*, 2011, **47**, 4102.
19. T. He, J. Wang, Z. Chen, A. Wu, G. Wu, J. Yin, H. Chu, Z. Xiong, T. Zhang and P. Chen, *J. Mater. Chem.*, 2012, **22**, 7478.
20. Y. J. Choi, Y. Xu, W. J. Shaw and E. C. E. Rönnebro, *The J. Phys. Chem. C*, 2012, **116**, 8349.
21. R. V. Genova, K. J. Fijalkowski, A. Budzianowski and W. Grochala, *J. Alloy Compd.*, 2010, **499**, 144.
22. H. V. K. Diyabalanage, T. Nakagawa, R. P. Shrestha, T. A. Semelsberger, B. L. Davis, B. L. Scott, A. K. Burrell, W. I. F. David, K. R. Ryan, M. O. Jones and P. P. Edwards, *J. Am. Chem. Soc.*, 2010, **132**, 11836.
23. Z. T. Xiong, C. K. Yong, G. T. Wu, P. Chen, W. Shaw, A. Karkamkar, T. Autrey, M. O. Jones, S. R. Johnson, P. P. Edwards and W. I. F. David, *Nat Mater*, 2008, **7**, 138-141.
24. G. L. Xia, X. B. Yu, Y. H. Guo, Z. Wu, C. Z. Yang, H. K. Liu and S. X. Dou, *Chem. Euro. J.*, 2010, **16**, 3763.
25. Z. Tang, Y. B. Tan, X. W. Chen and X. B. Yu, *Chem Commun*, 2012, **48**, 9296.
26. F. E. Pinkerton, *J. Alloys. Compd.*, 2011, **509**, 8958.
27. P. E. de Jongh, M. Allendorf, J. J. Vajo and C. Zlotea, *MRS Bulletin*, 2013, **38**, 488.
28. T. K. Nielsen, F. Besenbacher and T. R. Jensen, *Nanoscale*, 2011, **3**, 2086.
29. P. E. de Jongh and P. Adelhelm, *ChemSusChem*, 2010, **3**, 1332.
30. G. L. Xia, L. Li, Z. P. Guo, Q. F. Gu, Y. H. Guo, X. B. Yu, H. K. Liu and Z. W. Liu, *J. Mater. Chem. A*, 2013, **1**, 250.
31. G. L. Xia, Q. Meng, Z. P. Guo, Q. F. Gu, H. K. Liu, Z. W. Liu and X. B. Yu, *Acta Mater.*, 2013, **61**, 6882.
32. H. Wu, *ChemPhysChem*, 2008, **9**, 2157.
33. J. Gao, P. Ngene, I. Lindemann, O. Gutfleisch, K. P. de Jong and P. E. de Jongh, *J. Mater. Chem.*, 2012, **22**, 13209.
34. T. K. Nielsen, M. Polanski, D. Zasada, P. Javadian, F. Besenbacher, J. Bystrzycki, J. Skibsted and T. R. Jensen, *ACS Nano*, 2011, **5**, 4056.
35. P. Ngene, R. van den Berg, M. H. W. Verkuijlen, K. P. de Jong and P. E. de Jongh, *Energy Environ. Sci.*, 2011, **4**, 4108.
36. T. K. Nielsen, U. Bösenberg, R. Gosalawit, M. Dornheim, Y. Cerenius, F. Besenbacher and T. R. Jensen, *ACS Nano*, 2010, **4**, 3903.
37. T. K. Nielsen, K. Manickam, M. Hirscher, F. Besenbacher and T. R. Jensen, *ACS Nano*, 2009, **3**, 3521.
38. P. E. d. Jongh, R. W. P. Wagemans, T. M. Eggenhuisen, B. S. Dauvillier, P. B. Radstake, J. D. Meeldijk, J. W. Geus and K. P. d. Jong, *Chem. Mater.*, 2007, **19**, 6052.
39. G. Srinivas, W. Travis, J. Ford, H. Wu, Z.-X. Guo and T. Yildirim, *J. Mater. Chem. A*, 2013, **1**, 4167.
40. L. Gao, C.-Y. V. Li, H. Yung and K.-Y. Chan, *Chem. Comm.*, 2013, **49**, 10629.
41. Z. Li, G. Zhu, G. Lu, S. Qiu and X. Yao, *J. Am. Chem. Soc.*, 2010, **132**, 1490.
42. L. Li, X. Yao, C. Sun, A. Du, L. Cheng, Z. Zhu, C. Yu, J. Zou, S. C. Smith, P. Wang, H.-M. Cheng, R. L. Frost and G. Q. Lu, *Adv. Funct.Mater.*, 2009, **19**, 265.
43. T. Zhang, X. Yang, S. Yang, D. Li, F. Cheng, Z. Tao and J. Chen, *Phys.Chem. Chem. Phys.*, 2011, **13**, 18592.
44. G. Moussa, U. B. Demirci, S. Malo, S. Bernard and P. Miele, *J. Mater. Chem. A*, 2014, **2**, 7717.
45. M. L. Christian and K.-F. Aguey-Zinsou, *ACS Nano*, 2012, **6**, 7739.
46. G. L. Xia, D. Li, X. W. Chen, Y. B. Tan, Z. Tang, Z. P. Guo, H. K. Liu, Z. W. Liu and X. B. Yu, *Adv. Mater.*, 2013, **25**, 6238.
47. Z. Xiong, Y. Chua, G. Wu, L. Wang, M. W. Wong, Z. M. Kam, T. Autrey, T. Kemmitt and P. Chen, *Dalton Trans.*, 2010, **39**, 720.
48. Y. Wang and Z. X. Guo, *J. Mater. Chem. A*, 2014, **2**, 6801.
49. Z. W. Tang, S. F. Li, Z. X. Yang and X. B. Yu, *J. Mater. Chem.*, 2011, **21**, 14616.
50. S. Gadipelli, J. Ford, W. Zhou, H. Wu, T. J. Udovic and T. Yildirim, *Chem. Euro. J.*, 2011, **17**, 6043.
51. X. D. Kang, Z. Z. Fang, L. Y. Kong, H. M. Cheng, X. D. Yao, G. Q. Lu and P. Wang, *Adv. Mater.*, 2008, **20**, 2756.
52. K. Shimoda, Y. Zhang, T. Ichikawa, H. Miyaoka and Y. Kojima, *J. Mater. Chem.*, 2011, **21**, 2609.